

DOI:10.1002/ejic.201300624

# Hydrothermal Synthesis of Cu@C Composite Spheres by a One-Step Method and Their Use as Sacrificial Templates to Synthesize a CuO@SiO<sub>2</sub> Core–Shell Structure

Yi Cheng,<sup>[a]</sup> Xiaoyu Niu,<sup>[b]</sup> Tieying Zhao,<sup>[a]</sup> Fulong Yuan,<sup>\*[a]</sup>  
Yujun Zhu,<sup>\*[a]</sup> and Honggang Fu<sup>[a]</sup>

**Keywords:** Carbon / Copper / Hydrothermal synthesis / Core–shell structures / Composite spheres

Cu@C composite spheres with copper nanoparticles dispersed in the carbonaceous matter have been synthesized by a one-step hydrothermal method by using different copper salts mixed with an aqueous glucose solution. The spheres have been characterized by X-ray diffraction, scanning electron microscopy, transmission electron microscopy, thermogravimetric–differential thermal analysis, inductively coupled plasma atomic emission spectrometry, Fourier transform infrared spectroscopy, and Raman spectroscopy. The results show that Cu(NO<sub>3</sub>)<sub>2</sub>, CuSO<sub>4</sub>, and CuCl<sub>2</sub> exhibit an accelerating effect on the size of the composite spheres, and micro-

sized composites were obtained. However, a morphological change from irregular cubes and spheres to uniform spheres with a narrow size distribution of 340–400 nm was observed when cupric acetate [Cu(Ac)<sub>2</sub>] was used. Interestingly, Cu<sub>2</sub>O, generated in situ from Cu(ac)<sub>2</sub>, plays an important role in the size of the composite spheres. Moreover, a CuO@SiO<sub>2</sub> core–shell structure has been synthesized by using the Cu@C composite spheres as a sacrificial template, and the CO+NO reaction was used as a probe reaction to evaluate its catalytic performance. CuO@SiO<sub>2</sub> exhibits excellent catalytic performance in the CO+NO reaction.

## Introduction

Since the discovery of fullerenes in 1985 and carbon nanotubes in 1991,<sup>[1]</sup> the synthesis and application of carbon materials have received much attention, motivated by their potential environmental applications<sup>[2]</sup> and their use in electrodes,<sup>[3]</sup> catalyst supports, biological imaging, and as sacrificial templates for the fabrication of hollow or core–shell structures.<sup>[4]</sup> Therefore, many synthetic methods such as electronic arc-discharge, chemical vapor deposition, pyrolysis of organic compounds, and hydrothermal carbonization (HTC) have been developed for the preparation of different functional carbon materials.<sup>[5]</sup>

Among the various synthetic methods, the HTC of biomass is a promising candidate for the synthesis of functional carbonaceous materials owing to its simplicity, high efficiency, and sustainability.<sup>[6]</sup> When an aqueous solution

or dispersion of saccharides, organic compounds, or crude plant materials is hydrothermally treated, two types of products can be generated in the final reaction medium: water-soluble organic substances and insoluble residual solid products.<sup>[6,7]</sup> Generally, monodispersed carbonaceous spheres can be obtained when glucose,<sup>[7b,7c]</sup> sucrose,<sup>[7d]</sup> fructose,<sup>[8]</sup> cyclodextrins,<sup>[9]</sup> starch, or cellulose is used as the carbon source,<sup>[10]</sup> and their diameter can be easily modulated by variation of the synthetic parameters.<sup>[7d]</sup> Moreover, the obtained spheres usually have an intrinsic porous structure and abundant functional groups, which greatly widens their use in catalyst supports, biological applications, and sacrificial templates for the fabrication of hollow spheres such as Ga<sub>2</sub>O<sub>3</sub>, GaN,<sup>[4h]</sup> WO<sub>3</sub>,<sup>[4i]</sup> NiO, Co<sub>3</sub>O<sub>4</sub>, CeO<sub>2</sub>, and MFe<sub>2</sub>O<sub>4</sub> (M = Zn, Co, Ni, Cd) or rattle-type Fe<sub>3</sub>O<sub>4</sub>@SiO<sub>2</sub>.<sup>[11]</sup> In summary, the HTC process represents a cheap, easy, and sustainable route to carbonaceous materials from biomass.<sup>[6a,12]</sup>

On the other hand, composite structures that comprise nanoscaled metals or metal oxides and submicrometer dielectric spheres of materials such as silica, polystyrene, and carbon have attracted continuous research interest because of their potential applications in adsorbents, electrodes, biological imaging, drug delivery, and catalysis.<sup>[13]</sup> Colloidal carbonaceous spheres have received much attention because of their easy preparation, modulation, and green chemistry nature. Carbonaceous composites can be easily formed by

[a] Key Laboratory of Functional Inorganic Material Chemistry (Heilongjiang University), Ministry of Education, School of Chemistry and Materials, Heilongjiang University, Harbin 150080, China  
E-mail: fulongyuan2000@yahoo.com  
yujunzhu@hlju.edu.cn

[b] Key Laboratory of Chemical Engineering Process & Technology for High-Efficiency Conversion, College of Heilongjiang Province, School of Chemistry and Materials, Heilongjiang University, Harbin 150080, China

Supporting information for this article is available on the WWW under <http://dx.doi.org/10.1002/ejic.201300624>

a one-step HTC process in the presence of previously synthesized nanoparticles or water-soluble metal salts.<sup>[14]</sup> Sun and Li have reported an approach to monodisperse colloidal carbon spheres in the size range 150–1500 nm, which inherit the reactivity and hydrophilicity of the glucose starting material. Moreover, syntheses in which the noble-metal (Ag, Au, Pd, Pt) nanoparticles were loaded onto or encapsulated in carbon spheres to form hybrid structures have been investigated. Meanwhile, gold nanoparticles can be encapsulated in carbon by in situ hydrothermal reduction of noble-metal ions with glucose. In other words, carbon spheres containing one or two Au nanoparticle cores were obtained from hydrothermal reduction. Yu et al. reported the synthesis of  $\text{Fe}_x\text{O}_y@\text{C}$  spheres by a one-pot hydrothermal cohydrolysis–carbonization process.<sup>[14a]</sup> However, iron ions and metal oxide particles, as catalysts, are able to effectively accelerate the dehydration and carbonization of saccharides.<sup>[6a,14a,14c]</sup> Therefore, microsized composites are always obtained and these are unfavorable for mass transfer kinetics in catalysis and are unsuitable for the fabrication of core–shell structures. In consideration of the wide application of copper or copper oxide nanoparticles as catalysts,<sup>[15]</sup> it is necessary and interesting to synthesize smaller carbonaceous composites with copper or copper oxide nanoparticles. Unfortunately,  $\text{Cu}@\text{C}$  composites have not yet been reported.

Our present work is dedicated to the synthesis of  $\text{Cu}@\text{C}$  composites with copper nanoparticles dispersed in the carbonaceous spheres. In addition, a smaller  $\text{Cu}@\text{C}$  composite was used as a sacrificial template for the fabrication of a  $\text{CuO}@\text{SiO}_2$  core–shell structure, and the  $\text{CO} + \text{NO}$  reaction was used to evaluate its catalytic performance.

## Results and Discussion

### Synthesis and Characterization of $\text{Cu}@\text{C}$ Composite Spheres

The samples were obtained by using cupric acetate [ $\text{Cu}(\text{Ac})_2$ ] as the copper source under different reaction conditions. The XRD patterns of the samples obtained under different hydrothermal times (0.5, 3, 6 and 12 h) are shown in Figure 1 (the samples are denoted as  $\text{CuX}-t$ ;  $\text{CuX}$  represents the copper salt used in the synthetic process, and  $t$  represents the hydrothermal time [h]). The typical diffraction peaks at 29.4, 36.4, 42.0, 61.3, 73.3, and 77.1° (marked with solid circles) confirm the presence of  $\text{Cu}_2\text{O}$  (JCPDS Card No. 05–0667), whereas the peaks marked with squares are in good agreement with the standard literature values reported for Cu (JCPDS Card No. 04–0836). It is clear that the  $\text{Cu}_2\text{O}$  diffraction intensity in the  $\text{Cu}(\text{Ac})_2$ -0.5 sample is much stronger than those of the others. Meanwhile, the diffraction intensity of  $\text{Cu}_2\text{O}$  gradually decreases as the hydrothermal time increases from the  $\text{Cu}(\text{Ac})_2$ -0.5 to the  $\text{Cu}(\text{Ac})_2$ -12 sample. Eventually, the  $\text{Cu}_2\text{O}$  diffraction peak disappeared completely in the  $\text{Cu}(\text{Ac})_2$ -12 sample. Conversely, the Cu diffraction intensity is very weak in  $\text{Cu}(\text{Ac})_2$ -0.5 and increases significantly when the hydrother-

mal time is prolonged from 0.5 to 6 h. Therefore, the XRD results indicate the generation of  $\text{Cu}_2\text{O}$  in a relatively short hydrothermal time, and the formed  $\text{Cu}_2\text{O}$  is gradually reduced to Cu when the hydrothermal time is prolonged. In addition, weak and broad diffraction signals ( $2\theta = 10\text{--}30^\circ$ ) attributed to amorphous carbon are also observed in the XRD patterns of the  $\text{Cu}(\text{Ac})_2$ -6 and  $\text{Cu}(\text{Ac})_2$ -12 samples, which illustrate that the carbonaceous structure has been formed in them.

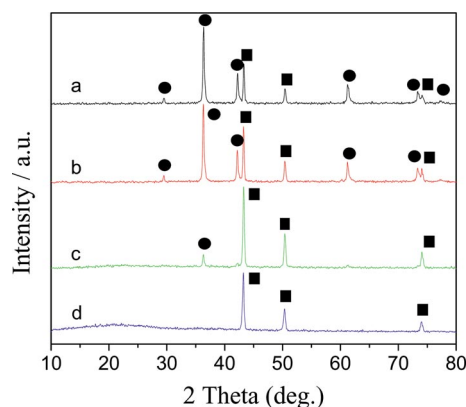


Figure 1. XRD patterns of (a)  $\text{Cu}(\text{Ac})_2$ -0.5, (b)  $\text{Cu}(\text{Ac})_2$ -3, (c)  $\text{Cu}(\text{Ac})_2$ -6, (d)  $\text{Cu}(\text{Ac})_2$ -12; ●  $\text{Cu}_2\text{O}$ , ■ Cu.

Furthermore, the copper content of the  $\text{Cu}(\text{Ac})_2$ - $t$  ( $t = 0.5, 3, 6$  and  $12$  h) samples was measured by inductively coupled plasma atomic emission spectroscopy (ICP-AES). Surprisingly, the copper contents of  $\text{Cu}(\text{Ac})_2$ -0.5 and  $\text{Cu}(\text{Ac})_2$ -3 were 86.10 and 86.35%, respectively. The corresponding  $\text{Cu}_2\text{O}$  mass fractions are 95.7 and 96.0%, respectively. Thus, XRD and ICP-AES results indicate that the main component is  $\text{Cu}_2\text{O}$  in the  $\text{Cu}(\text{Ac})_2$ -0.5 and  $\text{Cu}(\text{Ac})_2$ -3 samples. However, the copper contents of  $\text{Cu}(\text{Ac})_2$ -6 and  $\text{Cu}(\text{Ac})_2$ -12 were 34.65 and 11.54%, respectively, a decrease in comparison with those of  $\text{Cu}(\text{Ac})_2$ -0.5 and  $\text{Cu}(\text{Ac})_2$ -3. This explains why the Cu diffraction intensity of  $\text{Cu}(\text{Ac})_2$ -12 is weaker than that of  $\text{Cu}(\text{Ac})_2$ -6. The average amount of  $\text{Cu}(\text{Ac})_2$ -12 obtained was ca. 0.826 g when 18.9 mmol (3.75 g) of D-Glucose monohydrate ( $\text{C}_6\text{H}_{12}\text{O}_6 \cdot \text{H}_2\text{O}$ ) and 1.89 mmol (0.377 g) of cupric acetate monohydrate [ $\text{Cu}(\text{Ac})_2 \cdot \text{H}_2\text{O}$ ] were used as starting materials. The results mean that 79.4% of the copper in  $\text{Cu}(\text{Ac})_2 \cdot \text{H}_2\text{O}$  is converted in the  $\text{Cu}(\text{Ac})_2$ -12 sample.

The morphology and size of the samples was studied by SEM. It is clear that  $\text{Cu}(\text{Ac})_2$ -0.5 and  $\text{Cu}(\text{Ac})_2$ -3 show irregular cubes and spheres with a wide size distribution from 2 to 5  $\mu\text{m}$  as shown in Figure 2 (a and b). Based on their XRD and ICP results, these irregular cubes and spheres are the morphologies of  $\text{Cu}_2\text{O}$ . Pure  $\text{Cu}_2\text{O}$  particles exhibit morphologies such as cubes, spheres, octahedron shapes, and so on.<sup>[13e–13h,14–16]</sup> Under the current conditions, the continuous reduction of  $\text{Cu}_2\text{O}$  to Cu resulted in the formation of deformed spheres and cubes. However, the morphology of  $\text{Cu}(\text{Ac})_2$ -6 exhibits uniform spheres with smooth surfaces and a wide size distribution from 1.2 to 1.7  $\mu\text{m}$ , as

shown in Figure 2 (c and d). Based on previous reports<sup>[2a,7d]</sup> and our XRD results, we speculate that Cu@C composite spheres have been formed in Cu(Ac)<sub>2</sub>-6. This means that the concentration of aromatic clusters in the aqueous solution reaches the critical supersaturation point when the hydrothermal time is prolonged to 6 h. Therefore, a burst nucleation process occurs and microspheres are obtained.

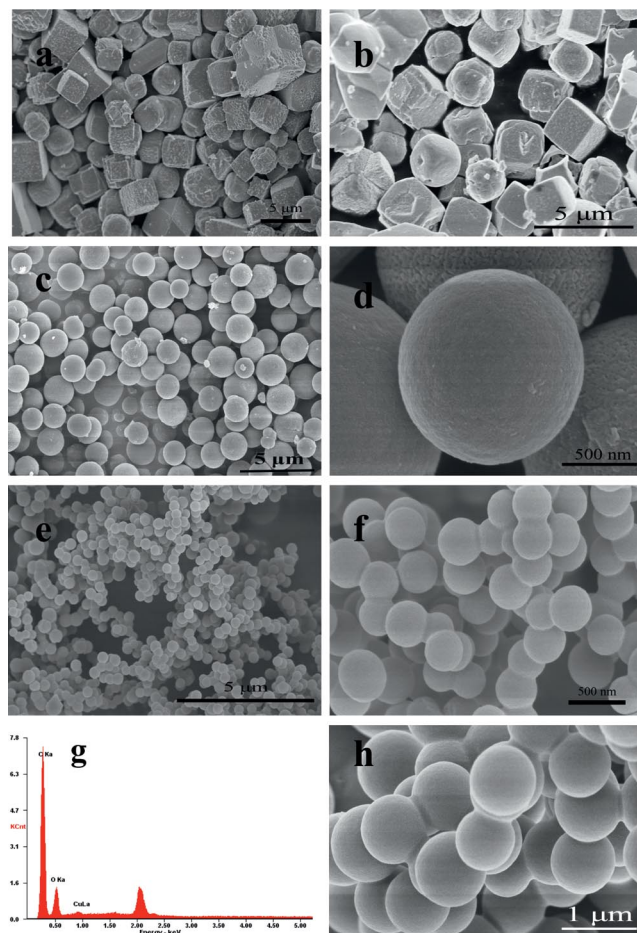


Figure 2. SEM images of (a) Cu(Ac)<sub>2</sub>-0.5, (b) Cu(Ac)<sub>2</sub>-3, (c and d) Cu(Ac)<sub>2</sub>-6, (e and f) Cu(Ac)<sub>2</sub>-12. (g) EDS spectrum of Cu(Ac)<sub>2</sub>-12 and (h) SEM image of CS-12.

Interestingly, when the reaction time was further prolonged to 12 h, submicron spheres were obtained with smooth surfaces and a considerably narrow size distribution from 340 to 400 nm, as shown in Figure 2 (e and f). The average diameter of the obtained spheres is 370 nm for the Cu(Ac)<sub>2</sub>-12 sample. Additionally, its corresponding energy dispersive X-ray spectroscopy (EDS) results reveal the presence of Cu, C, and O, which further demonstrates the formation of a composite structure. In our opinion, the decrease in the diameter of the composite spheres from 1.4 μm [Cu(Ac)<sub>2</sub>-6] to 370 nm [Cu(Ac)<sub>2</sub>-12] may be caused by the loosely crossed-linked outer structure of Cu(Ac)<sub>2</sub>-6. In other words, when the hydrothermal time was prolonged from 6 to 12 h, the loosely crossed-linked outer structure fractured and submicron spheres were obtained.<sup>[2a,4h]</sup> On the other hand, the Brunauer–Emmett–Teller (BET) spe-

cific surface area decreases from 8.0 to 4.5 m<sup>2</sup>g<sup>-1</sup>, which means that densification occurs for the Cu(Ac)<sub>2</sub>-6 sample in the HTC process. In summary, a morphological change from irregular cubes and spheres to uniform spheres is observed in the formation process of Cu@C composite spheres.

For comparison, we also synthesized carbon spheres at 180 °C for 12 h (denoted as CS-12), and their SEM image is shown in Figure 2 (h). The spheres have a smooth surface, and their mean diameter is ca. 850 nm. Some spheres have fused peanut shapes, and their diameter is two times larger than that of Cu(Ac)<sub>2</sub>-12. Therefore, the presence of Cu(Ac)<sub>2</sub> is favorable for the formation of smaller composite spheres in our synthesis process.

TEM measurements were also performed to unveil the detailed structure of Cu(Ac)<sub>2</sub>-12. The image is shown in Figure 3 (a). It is clear that the sample is composed of uniform solid spheres with smooth surfaces and a considerably narrow size distribution; the mean diameter is ca. 370 nm, which is consistent with the SEM result. Moreover, to unveil the detailed structure of Cu(Ac)<sub>2</sub>-12, HR-TEM was also performed (Figure 3, b). Lattice fringes, which can be attributed to the (111) plane of face-centered cubic copper, are observed.<sup>[17]</sup> Therefore, HR-TEM reveals that copper nanoparticles with a mean diameter of ca. 10 nm have been dispersed in the carbonaceous matter.

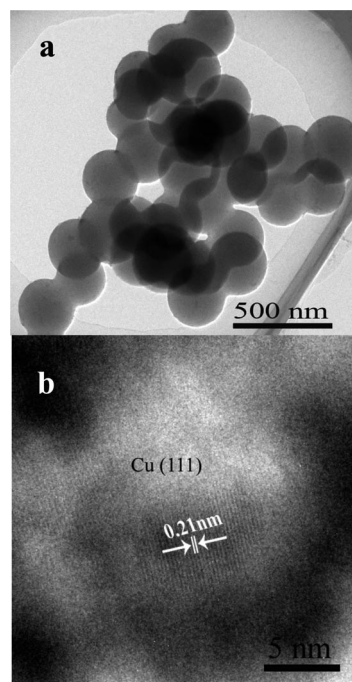


Figure 3. (a) TEM and (b) HR-TEM images of Cu(Ac)<sub>2</sub>-12.

Figure 4 shows the thermogravimetric–differential thermal analysis (TG-DTA) profiles of the materials obtained under different hydrothermal times. The TG curve of Cu(Ac)<sub>2</sub>-0.5 (Figure 4, a) shows very little weight loss (ca. 0.61%) before 370 °C, which may be caused by oxidation of the impurities wrapped in it. After that, a continuous weight increment process is followed, accompanied by a

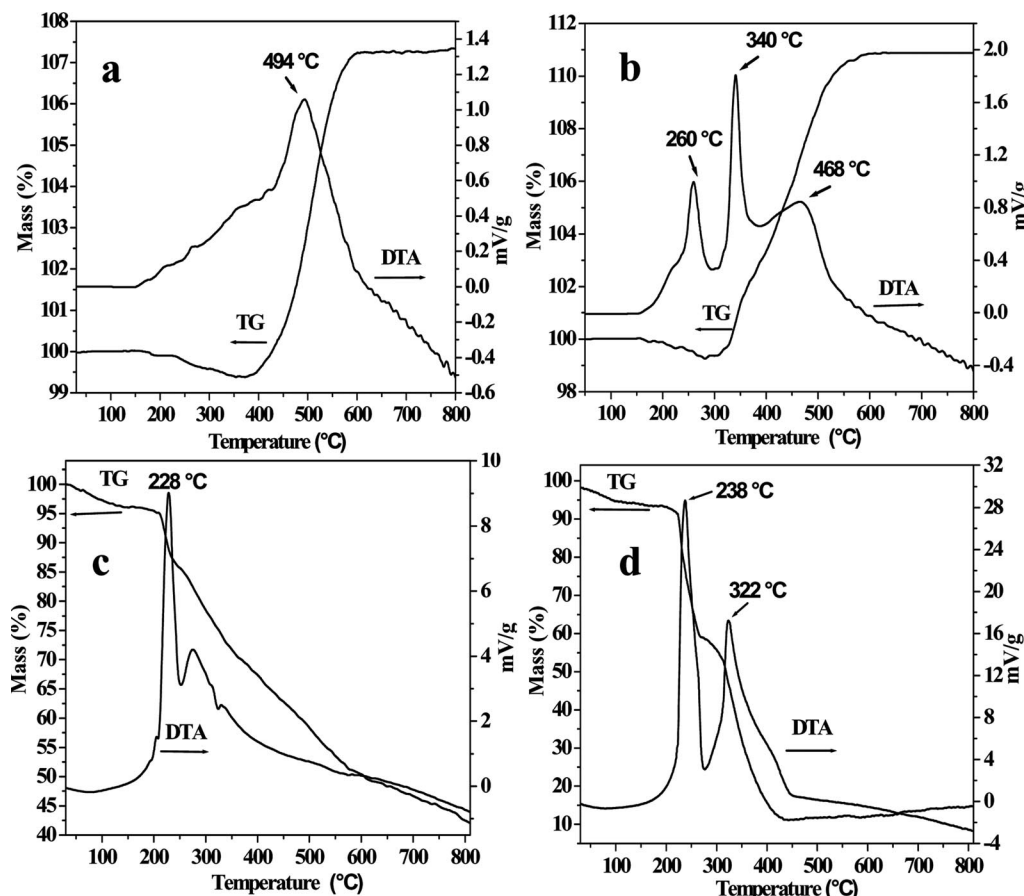


Figure 4. TG-DTA profiles of (a)  $\text{Cu}(\text{Ac})_2\text{-}0.5$ , (b)  $\text{Cu}(\text{Ac})_2\text{-}3$ , (c)  $\text{Cu}(\text{Ac})_2\text{-}6$ , and (d)  $\text{Cu}(\text{Ac})_2\text{-}12$ .

broad exothermic peak in the DTA curve at 494 °C, which may be attributed to the oxidations of Cu to  $\text{Cu}_2\text{O}$  and  $\text{Cu}_2\text{O}$  to CuO. Notably, Cu and  $\text{Cu}_2\text{O}$  were eventually oxidized to CuO, as confirmed by XRD (JCPDS Card No. 05–0661, Figure S1a in the Supporting Information). For  $\text{Cu}(\text{Ac})_2\text{-}3$ , the DTA curve (Figure 4, b) shows two exothermic peaks at 340 and 468 °C, which are attributed to the oxidations of Cu to  $\text{Cu}_2\text{O}$  and  $\text{Cu}_2\text{O}$  to CuO, respectively. From the TG curve, the weight loss is also only 0.74% in the range 30–280 °C for  $\text{Cu}(\text{Ac})_2\text{-}3$ . Therefore, the TG-DTA analysis reveals that the carbon contents of  $\text{Cu}(\text{Ac})_2\text{-}0.5$  and  $\text{Cu}(\text{Ac})_2\text{-}3$  are very low, which is consistent with the ICP-AES results and further confirms our hypothesis.

In contrast to those of  $\text{Cu}(\text{Ac})_2\text{-}0.5$  and  $\text{Cu}(\text{Ac})_2\text{-}3$ , the TG curve of  $\text{Cu}(\text{Ac})_2\text{-}6$  (Figure 4, c) shows a slow weight loss below 200 °C (4.9%), which may be caused by the desorption of physisorbed water. A continuous weight loss occurs above 200 °C, accompanied by a sharp exothermic peak at 228 °C, which can be attributed to the further dehydration and densification of the composite spheres. A broad exothermic peak follows and is attributable to the burning of the composite spheres.<sup>[4h]</sup> The final residual weight is 46.5%. Therefore, thermal analysis indicates that the carbon content in  $\text{Cu}(\text{Ac})_2\text{-}6$  is much more than those of  $\text{Cu}(\text{Ac})_2\text{-}0.5$  and  $\text{Cu}(\text{Ac})_2\text{-}3$ . The TG and DTA curves of  $\text{Cu}(\text{Ac})_2\text{-}12$  are similar to those of  $\text{Cu}(\text{Ac})_2\text{-}6$  below 450 °C.

However, a slight increase in weight is observed in the higher temperature region, and the final residual weight is 14.5%. Notably, the copper nanoparticles in  $\text{Cu}(\text{Ac})_2\text{-}12$  were eventually oxidized to CuO, as confirmed by XRD (JCPDS Card No. 05–0661, Figure S1b). The residual weight is 11.58% Cu content, which agrees well with the ICP result.

The chemical structures of the materials obtained under different hydrothermal times were investigated by FTIR and Raman spectroscopy. To facilitate our interpretation, the FTIR and Raman spectra of CS-12 were also recorded and are used as a reference. The relevant FTIR spectra are shown in Figure 5. The spectra of  $\text{Cu}(\text{Ac})_2\text{-}0.5$  and  $\text{Cu}(\text{Ac})_2\text{-}3$  show strong characteristic absorption bands at ca. 620  $\text{cm}^{-1}$ , which are attributed to the  $\text{Cu}^{\text{I}}\text{-O}$  deformation vibration.<sup>[16e,18]</sup> This further confirms the existence of  $\text{Cu}_2\text{O}$  and is consistent with the XRD results. In addition, they show very broad absorption bands at 800–4000  $\text{cm}^{-1}$ , which are assigned to the incorporation of impurities derived from the incomplete dehydration and carbonization of glucose. Surprisingly, the spectrum of  $\text{Cu}(\text{Ac})_2\text{-}6$  shows not only a weak  $\text{Cu}^{\text{I}}\text{-O}$  absorption band but also some characteristic absorption peaks that can be assigned to O–H (hydroxy or carboxyl) stretching (3000–3700  $\text{cm}^{-1}$ ), C=O stretching (1710  $\text{cm}^{-1}$ ), C=C (1620 and 1514  $\text{cm}^{-1}$ ), aliphatic hydrocarbon CH (2920  $\text{cm}^{-1}$ ), C–O (hydroxy, ester,

or ether) stretching and O–H bending vibrations (1000–1470  $\text{cm}^{-1}$ ). In addition, the band at 875–750  $\text{cm}^{-1}$  is assigned to the aromatic C–H out-of-plane bending vibration, which reveals C–H aromatization in the  $\text{Cu}(\text{Ac})_2$ -6 sample.<sup>[2d,7d,19]</sup> It is clear that the spectra of  $\text{Cu}(\text{Ac})_2$ -12 and CS-12 are similar to that of  $\text{Cu}(\text{Ac})_2$ -6 except for the disappearance of the characteristic  $\text{Cu}^{\text{I}}\text{–O}$  absorption band, which indicates they have a similar structure. In summary, the FTIR results indicate that there are abundant functional groups, such as hydroxy and carbonyl groups, on the surfaces of the composite spheres and this may widen their applications in catalysis or as templates for the fabrication of core–shell structures.<sup>[11c,11d]</sup>

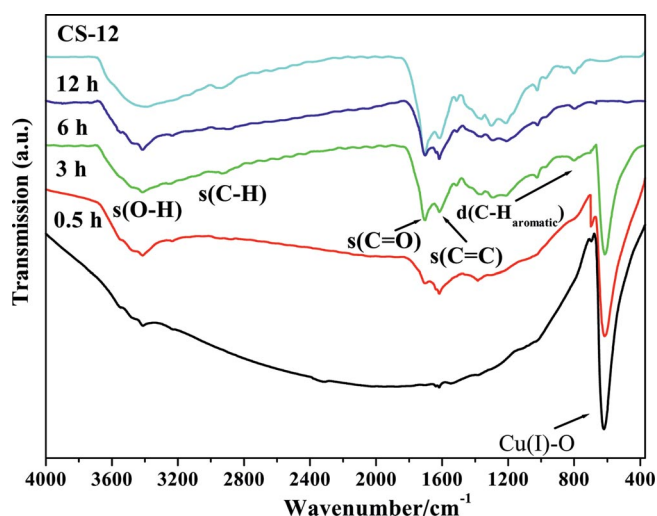


Figure 5. FTIR spectra of (a)  $\text{Cu}(\text{Ac})_2$ -0.5, (b)  $\text{Cu}(\text{Ac})_2$ -3, (c)  $\text{Cu}(\text{Ac})_2$ -6, (d)  $\text{Cu}(\text{Ac})_2$ -12, (e) CS-12; s = stretching vibration, d = deformation or bending vibration.

The Raman spectra of  $\text{Cu}(\text{Ac})_2$ -*t* (*t* = 0.5, 3, 6, and 12 h) samples are shown in Figure 6. The spectra of  $\text{Cu}(\text{Ac})_2$ -0.5 and  $\text{Cu}(\text{Ac})_2$ -3 only show two scattering peaks at ca. 280 and 610  $\text{cm}^{-1}$ , which are characteristic  $\text{Cu}_2\text{O}$  scattering peaks<sup>[20]</sup> and further confirm the existence of  $\text{Cu}_2\text{O}$  in these two samples, in good agreement with the XRD and IR results. However, the spectrum of  $\text{Cu}(\text{Ac})_2$ -6 shows not only weak scattering peaks attributable to  $\text{Cu}_2\text{O}$  but also two broad overlapping bands at ca. 1360 and 1590  $\text{cm}^{-1}$ , which are well known as the D and G bands of carbonized materials<sup>[21]</sup> and correspond to the  $E_{2g}$  mode of graphite layers and the vibrations of carbon atoms with dangling bonds in plane terminations of disordered graphite, respectively.<sup>[6a,10a,19]</sup> In addition, the pronounced bands in the 2400–3600  $\text{cm}^{-1}$  range can be assigned to  $\text{sp}^3$  C–H<sub>x</sub> stretching modes and 2G peaks.<sup>[6a,10b]</sup> Therefore, the Raman spectrum reveals the existence of small aromatic clusters in  $\text{Cu}(\text{Ac})_2$ -6, which agrees well with the aromatization observed in its IR spectra. Furthermore, the spectra of  $\text{Cu}(\text{Ac})_2$ -12 and CS-12 are similar to that of  $\text{Cu}(\text{Ac})_2$ -6 except for the disappearance of the characteristic  $\text{Cu}^{\text{I}}\text{–O}$  scattering peaks. Thus, the Raman spectra are consistent with the IR results.

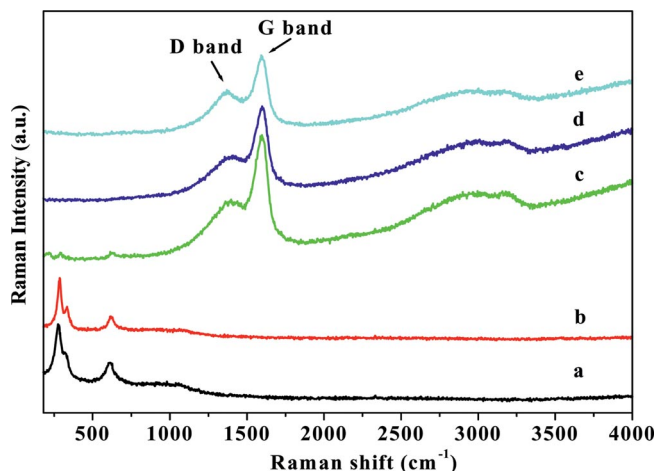


Figure 6. Raman spectra of (a)  $\text{Cu}(\text{Ac})_2$ -0.5, (b)  $\text{Cu}(\text{Ac})_2$ -3, (c)  $\text{Cu}(\text{Ac})_2$ -6, and (d)  $\text{Cu}(\text{Ac})_2$ -12, and (e) CS-12.

Notably, the diameter of the  $\text{Cu}@\text{C}$  composite spheres can be modulated by modifying the synthesis conditions with  $\text{Cu}(\text{ac})_2$  as the copper source. The most representative example is an increase of the molar ratio of cupric acetate to glucose from 1:10 to 1:5. The process to change the copper species and the morphology of the obtained materials is similar to the case of 1:10 discussed above (Figures S2 and S3). However, the obtained composite spheres always possess a much larger size. For example, the material obtained at 180 °C for 12 h has a mean diameter of 820 nm (Figure S3d). Furthermore, the hydrothermal temperature and type of saccharide (e.g., sucrose and starch) also have a significant effect on the size of the obtained composite spheres (see Figures S4 and S5). The material obtained at 200 °C for 12 h shows a wide size distribution from 1.6 to 2.1  $\mu\text{m}$ , which is much larger than the diameter of  $\text{Cu}(\text{ac})_2$ -12. In addition, microsized spheres could also be obtained when sucrose or starch was used as the carbon source and hydrothermally treated with  $\text{Cu}(\text{ac})_2$  at 180 °C for 12 h. However, their diameter is much larger than that of  $\text{Cu}(\text{ac})_2$ -12, which may be caused by their disaccharide and polysaccharide nature.

Other copper salt such as  $\text{Cu}(\text{NO}_3)_2$ ,  $\text{CuSO}_4$ , and  $\text{CuCl}_2$  were also used as the copper source to prepare the  $\text{Cu}@\text{C}$  composite. Unexpectedly, only red-brown solutions could be obtained when the hydrothermal time was less than 3 h. However, the liquid viscosity increased significantly, which means that aromatic compounds and oligosaccharides formed.<sup>[2a,7b]</sup> When the hydrothermal time was longer than 3 h, solid products could be obtained. Figure S6 shows the corresponding XRD patterns of the materials obtained at 180 °C for 3 and 12 h. Surprisingly, three characteristic diffraction peaks can be observed in  $\text{Cu}(\text{NO}_3)_2$ -3,  $\text{CuSO}_4$ -3,  $\text{Cu}(\text{NO}_3)_2$ -12, and  $\text{CuSO}_4$ -12, and they are in good agreement with the standard literature values reported for Cu (JCPDS Card No. 04-0836). In contrast, the diffraction peaks of  $\text{CuCl}_2$ -3 and  $\text{CuCl}_2$ -12 are in good agreement with those of CuCl (JCPDS Card No. 06-0344). Interestingly, even though the mixture was only hydrothermally treated

for 3 h, no diffraction signals attributable to  $\text{Cu}_2\text{O}$  are observed. Therefore, the XRD results reveal that  $\text{Cu}^{2+}$  is quickly reduced to Cu when  $\text{Cu}(\text{NO}_3)_2$  or  $\text{CuSO}_4$  is used, whereas if  $\text{CuCl}_2$  is used, the reduction product is  $\text{CuCl}$ , which may be caused by the insolubility of  $\text{CuCl}$ . In addition, weak and broad diffraction peaks ( $2\theta = 10\text{--}30^\circ$ ) attributed to amorphous carbon are also observed and indicate that the carbonaceous structure is formed in the materials after 3 h.

The SEM images of the materials synthesized with  $\text{Cu}(\text{NO}_3)_2$ ,  $\text{CuSO}_4$ , and  $\text{CuCl}_2$  as the copper source are shown in Figure 7. All of the materials exhibit spherical morphologies with wide size distributions of 2–6  $\mu\text{m}$  and tend to fuse to form particles with peanutlike and other irregular shapes. In addition, some submicron spheres are also observed. Notably,  $\text{Cu}(\text{NO}_3)_2$ ,  $\text{CuSO}_4$ , and  $\text{CuCl}_2$  have no significant effect on the size of the corresponding material, and the diameter of the spheres increases only slightly although the hydrothermal time was prolonged from 3 to 12 h. Therefore, the SEM results indicate that these copper salts can drastically accelerate the dehydration and carbonization of glucose. As a result, the concentration of aromatic clusters in the aqueous solution reaches the critical supersaturation point quickly and a burst nucleation process occurs. Thereby, microscaled composite spheres could be obtained with hydrothermal treatment for only 3 h.

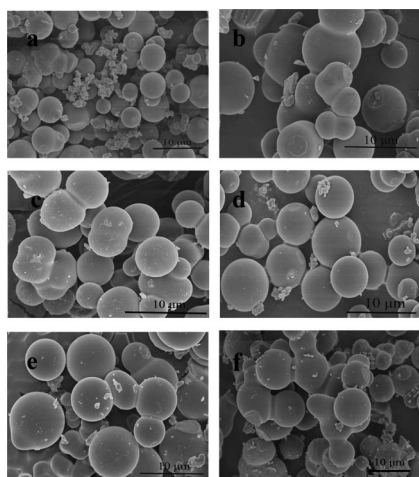


Figure 7. SEM images of the materials obtained by using  $\text{Cu}(\text{NO}_3)_2$ ,  $\text{CuSO}_4$ , and  $\text{CuCl}_2$  as copper source. (a)  $\text{Cu}(\text{NO}_3)_2$ -3, (b)  $\text{Cu}(\text{NO}_3)_2$ -12, (c)  $\text{CuSO}_4$ -3, (d)  $\text{CuSO}_4$ -12, (e)  $\text{CuCl}_2$ -3, and (f)  $\text{CuCl}_2$ -12.

The TG-DTA and the IR and Raman spectra further confirm the XRD results. The TG-DTA results (Figure S7) reveal that different copper salts have a significant effect on the carbon content of the corresponding materials. Moreover, the carbon content of the obtained materials also increases when the hydrothermal time is prolonged. The change tendency is consistent with the ICP-AES results presented in Table S1. The FTIR spectra of these materials (Figure S8) show no characteristic  $\text{Cu}^{\text{I}}\text{--O}$  absorption bands, which confirms that  $\text{Cu}_2\text{O}$  does not exist in these materials and is in good agreement with their XRD results.

Similarly, there are abundant functional groups on the surfaces of these composite spheres, and the main characteristic absorption peaks can be assigned to O–H, C–H, C=O, C=C, and C–H vibration bands, as shown in Figure S8a. The Raman spectra of these materials are shown in Figure S9. The two scattering peaks at ca. 1360 and 1590  $\text{cm}^{-1}$  are typical signals of carbonized materials, known as D and G bands, respectively. Therefore, the Raman spectra confirm the existence of small aromatic clusters in these composites, which agrees well with the aromatization of these materials as revealed by their FTIR spectra (Figure S8). Furthermore, no scattering peaks can be assigned to  $\text{Cu}_2\text{O}$ , which indicates that  $\text{Cu}_2\text{O}$  does not exist in these materials. Thus, these results reveal that  $\text{Cu}(\text{NO}_3)_2$ ,  $\text{CuSO}_4$ , and  $\text{CuCl}_2$  can drastically accelerate the dehydration and carbonization of glucose.

When  $\text{Cu}(\text{NO}_3)_2$ ,  $\text{CuSO}_4$ , and  $\text{CuCl}_2$  were used as the copper source,  $\text{Cu}_2\text{O}$  did not exist in the obtained materials as proved by XRD and IR and Raman spectroscopy. We speculate that this phenomenon may be caused by their different reduction potentials. The concentration of free  $\text{Cu}^{2+}$  in the initial solution with  $\text{Cu}(\text{Ac})_2$  as the copper source is lower than that of with the other copper salts, as the acetate anion is a monodentate ligand. For  $\text{Cu}(\text{NO}_3)_2$  and  $\text{CuSO}_4$ , the glucose dehydration and fragmentation rates are drastically accelerated, which results in an increase in the amount of reducing agent. Thus, the formed unstable  $\text{Cu}_2\text{O}$  can be quickly reduced to Cu, and microscaled  $\text{Cu}_2\text{O}$  cannot be obtained. In summary, microscaled  $\text{Cu}_2\text{O}$  is generated from  $\text{Cu}(\text{Ac})_2$  and its heterogeneous reduction leads to the formation of submicron  $\text{Cu@C}$  composite spheres, whereas microscaled  $\text{Cu@C}$  composite spheres can be obtained when  $\text{Cu}(\text{NO}_3)_2$ ,  $\text{CuSO}_4$ , or  $\text{CuCl}_2$  is used as the copper source.

### Formation Process of $\text{Cu@C}$ Composite Spheres

Based on the above results and discussion, a possible formation process for  $\text{Cu@C}$  composite spheres obtained with  $\text{Cu}(\text{Ac})_2$  as the copper source is proposed and is illustrated in Figure 8. Step I is the homogeneous reduction of  $\text{Cu}^{2+}$  to microscaled  $\text{Cu}_2\text{O}$ , in which  $\text{Cu}(\text{Ac})_2$  is effectively reduced by glucose and its dehydration and fragmentation products; this is a homogeneous reaction and its main product is  $\text{Cu}_2\text{O}$ , as confirmed by the XRD results. The formed  $\text{Cu}_2\text{O}$  is composed of irregular spheres and cubes with sizes over 2  $\mu\text{m}$ , as measured by SEM, as the  $\text{Cu}^{2+}$  is reduced quickly by glucose in the initial stage (step I). In step II, the heterogeneous reduction of  $\text{Cu}_2\text{O}$  and nucleation results in the formation of microscaled spheres. The pH of the mixture before hydrothermal treatment is 5.65. However, the pH of the solutions decreased to 3.25 and 2.77 after hydrothermal treatment at 180  $^\circ\text{C}$  for 0.5 and 3 h, respectively.  $\text{Cu}_2\text{O}$  is unstable in acidic solution and can be further reduced by the residual glucose as well as its dehydration and fragmentation products. The reduction of  $\text{Cu}_2\text{O}$  changes from a homogeneous reaction to a heterogeneous reaction owing to the formation of microscaled irregular spheres and cubes.

Thus, a decrease of the reaction rate of step II relative to step I is predicted and can be concluded from the presence of a small amount of  $\text{Cu}_2\text{O}$  in  $\text{Cu}(\text{Ac})_2$ . Meanwhile, the pH of the solution decreases to 2.55. When the concentration of aromatic clusters (dehydration and fragmentation products of glucose) reaches the critical supersaturation point after 3 h, the nucleation process can occur and micro-sized spheres form in step II.<sup>[7d,14a]</sup> The residual  $\text{Cu}_2\text{O}$  is totally reduced to Cu, and densification of the formed microspheres occurs when the reaction time is longer than 6 h. Finally, nanospheres with a mean diameter of 370 nm are obtained (step III), and the copper nanoparticles are dispersed in the carbonaceous matter.

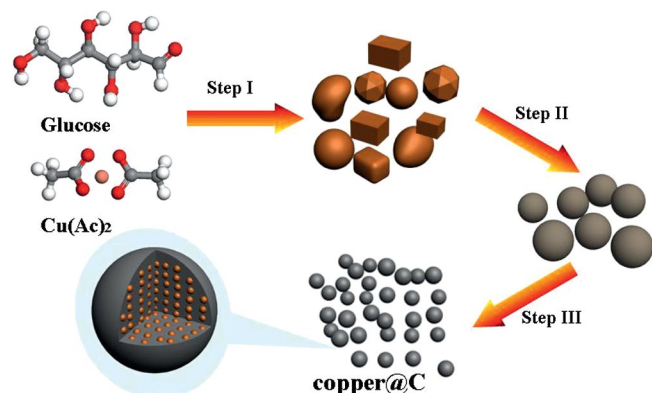


Figure 8. Formation process of  $\text{Cu}@C$  composites with  $\text{Cu}(\text{Ac})_2$  as copper source.

Our method is similar to that of Sun and Li. However, the experimental results are different. According to the experiments of Sun,<sup>[7b]</sup> Au-cored carbon spheres are obtained from hydrothermal reduction. The diameter of the carbon spheres is ca. 450 nm, and the diameter of the noble-metal nanoparticles could be manipulated in the range 8–50 nm. In contrast, solid carbon spheres with Cu nanoparticles dispersed in them rather than Cu-cored carbon sphere core-shell structures are obtained in our experiments. When  $\text{Cu}(\text{ac})_2$  is used as the copper source, the  $\text{Cu}@C$  composite spheres are uniform solid spheres with a narrow size of 340–400 nm, and copper nanoparticles with a mean diameter of ca. 10 nm are dispersed in the carbonaceous matter. Therefore, the products and their formation process are different, although the synthesis methods are similar.

### Synthesis of a $\text{CuO}@SiO_2$ Core-Shell Structure from $\text{Cu}@C$ Composite Spheres and Its Catalytic Performance

The  $\text{Cu}@C$  composite spheres possess a very low surface area [ $4.5 \text{ m}^2 \text{ g}^{-1}$  for  $\text{Cu}(\text{Ac})_2$ -12], which limits their application as catalysts. However, the  $\text{Cu}@C$  composite spheres are excellent templates for the synthesis of core-shell structures with high surface areas owing to the abundant functional groups on their surfaces.<sup>[11c]</sup> Here, a core-shell structured material ( $\text{CuO}@SiO_2$ ) with a CuO core and silica shell could be obtained by using  $\text{Cu}(\text{Ac})_2$ -12 as a sacrificial template. Figure 9 shows the XRD pattern of the

$\text{CuO}@SiO_2$  sample. The result indicates that the copper species in the material is monoclinic CuO (JCPDS Card No. 05–0661), which means zero-valent Cu is completely oxidized to CuO in the preparation process. In addition, a diffraction signal attributable to amorphous silica is also detected in the  $2\theta$  range 10–30°.

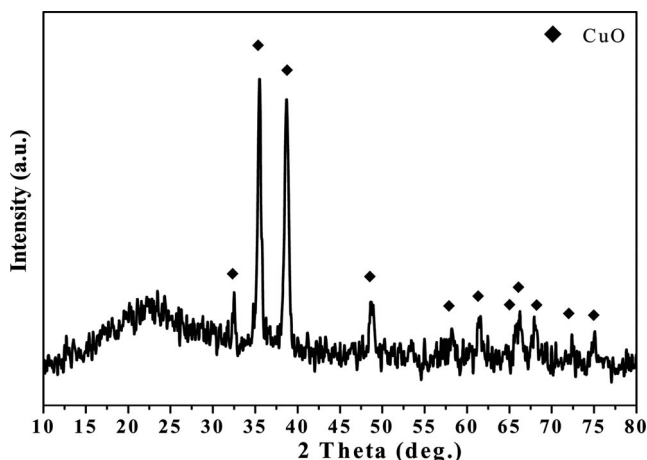


Figure 9. XRD pattern of the  $\text{CuO}@SiO_2$  core-shell structure.

Figure 10a shows the SEM image of the  $\text{CuO}@SiO_2$  precursor. By comparison with the SEM image of  $\text{Cu}(\text{Ac})_2$ -12 sample, it can be seen that the  $\text{Cu}@C$  composite spheres are well coated with silica precursor (tetraethyl orthosilicate, TEOS). The mean diameter is ca. 500 nm, and the coarse shell is made up of unequal nanosized spheres of the hydrolyzate of TEOS; the thickness is calculated to be 130 nm. Interestingly, open-mouthed spheres could be obtained after calcination, and a coarse shell that consists of nanoparticles is observed (Figure 10, b). The TEM image is shown in Figure 10c. A clear core-shell structure with a coarse shell is observed. The corresponding nitrogen adsorption-desorption isotherm is shown in Figure 10d. A typical type IV isotherm indicates its mesoporous character, and the pore diameter is 2 nm.<sup>[22]</sup> The BET surface area is  $64.5 \text{ m}^2 \text{ g}^{-1}$ . Therefore, the results of XRD, TEM, and nitrogen adsorption-desorption demonstrate that a  $\text{CuO}@SiO_2$  core-shell with a mesoporous shell was successfully synthesized.

The catalytic performance of the  $\text{CuO}@SiO_2$  was evaluated for the CO+NO reaction. Figure 11 shows the NO conversion and  $\text{N}_2$  yield over the  $\text{CuO}@SiO_2$  catalyst as a function of temperature. For the fresh  $\text{CuO}@SiO_2$  catalyst (Figure 11, Run 1), the conversion of NO was ca. 10% at 100 °C. Notably, above 100 °C, the NO conversion increased dramatically and reached 100% at 180 °C. The  $\text{N}_2$  yield was 94.2% at 180 °C, and 100%  $\text{N}_2$  yield was attained at 250 °C. The activity of the  $\text{CuO}@SiO_2$  catalyst is especially high compared to those of copper-containing catalysts for the NO+CO reaction. In addition, the catalytic performance of the  $\text{CuO}@SiO_2$  was also evaluated after Run 1 without any treatment. The catalytic performance of the used  $\text{CuO}@SiO_2$  catalyst (Figure 11, Run 2) does not decrease. Moreover, the activity is higher than that for Run

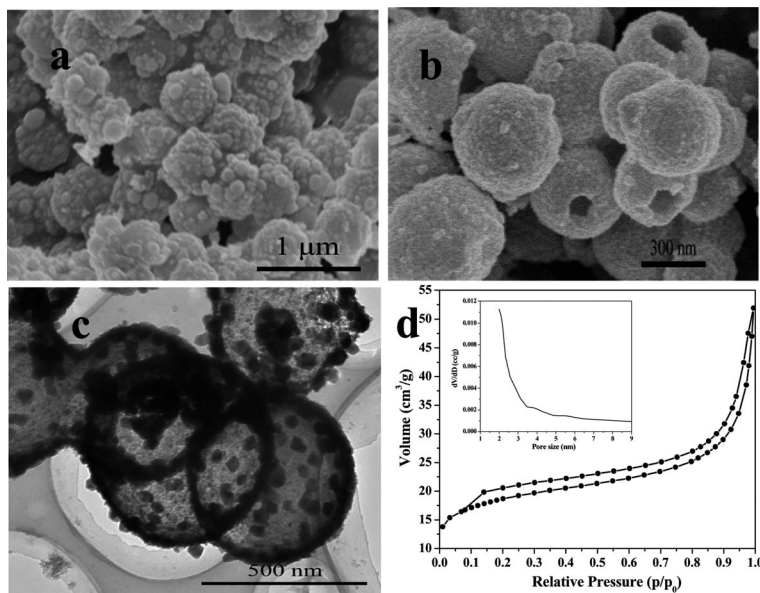


Figure 10. SEM images of (a) silica-coated precursor and (b) CuO@SiO<sub>2</sub> core-shell structure. (c) TEM image of the CuO@SiO<sub>2</sub> core-shell structure. (d) Nitrogen adsorption-desorption isotherm of the CuO@SiO<sub>2</sub> core-shell structure (the inset is the pore size distribution).

1, but the temperature for the complete conversion of NO is still maintained at 180 °C in Run 2. Therefore, the

CuO@SiO<sub>2</sub> core-shell structure exhibits an excellent catalytic performance in the CO + NO reaction.

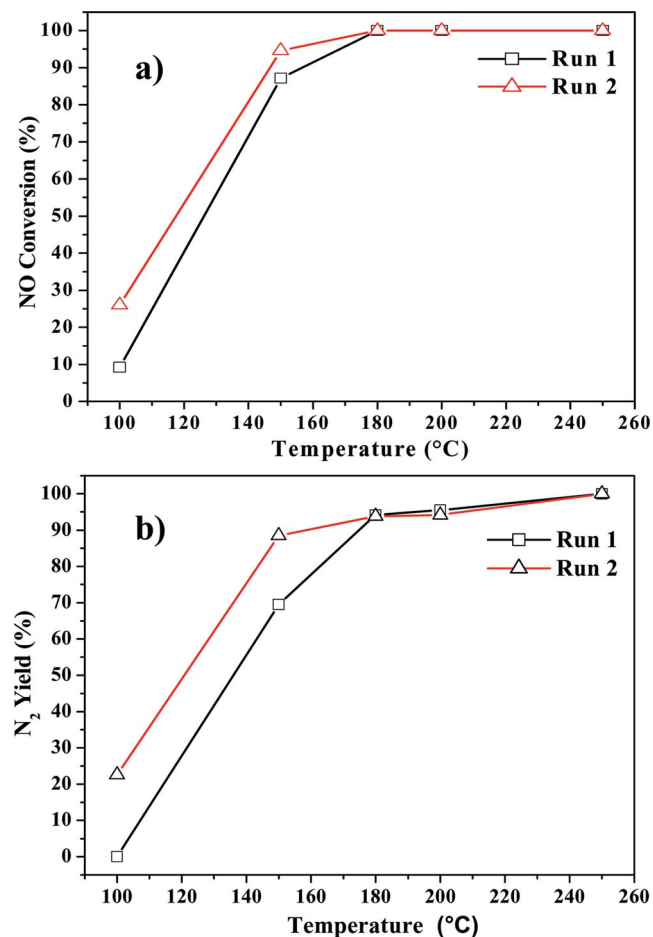


Figure 11. (a) The NO conversion and (b) N<sub>2</sub> yield over the CuO@SiO<sub>2</sub> catalyst in the CO + NO reaction.

## Conclusions

Submicron Cu@C composite spheres have been successfully synthesized by a one-step method. In situ generated micro-sized cuprous oxide exhibits a special effect on the size of the composite spheres when Cu(ac)<sub>2</sub> is used as the copper source, whereas other copper salts such as Cu(NO<sub>3</sub>)<sub>2</sub>, CuSO<sub>4</sub>, and CuCl<sub>2</sub> can drastically accelerate the dehydration and carbonization of glucose and lead to the formation of micro-sized Cu@C composites. Furthermore, a CuO@SiO<sub>2</sub> core-shell structure is successfully synthesized by using the Cu@C composite spheres as sacrificial templates, and they exhibit excellent catalytic performance in the CO + NO reaction; N<sub>2</sub> yields of 94.2 and 100% are attained at 180 and 250 °C, respectively. Thus, this method provides an efficient route to synthesis of core-shell structure catalysts.

## Experimental Section

**Experimental Details:** All chemicals were analytical grade and were purchased from Tianjin Kermel Chemical Reagents Development Centre and used without further purification.

**Materials Characterization:** The X-ray diffraction (XRD) patterns were obtained with a D/MAX-3B X-ray diffractometer (Rigaku Co.) at room temperature with Ni-filtered Cu-K<sub>α</sub> radiation (λ = 1.54056 Å). The particle size and morphologies were observed by scanning electron microscopy (SEM) with a Hitachi S-4800 field emission electron microscope operating at 5.0 kV. Transmission electron microscopy (TEM) images were obtained with a JEOL 2010 electron microscope operating at 200 kV. The Raman spectra was recorded with a JY HR800 Raman spectrometer with an ar-

gon-ion laser at an excitation wavelength of 514.5 nm at room temperature. The Fourier transform infrared spectroscopy (FTIR) spectra were recorded with a Perkin–Elmer Spectrum one FTIR Spectrometer. The samples were prepared by pressing the solid materials with KBr. The thermogravimetric–differential thermal analysis (TG-DTA) profiles were recorded with a HCT-1 thermal analyzer at a heating rate of 10 °C min<sup>-1</sup> from room temperature to 800 °C in static atmosphere. The Brunauer–Emmett–Teller (BET) specific surface area was measured according to nitrogen adsorption at 77 K by using a Micromeritics Tristar 3020 physisorption instrument. The copper content of the prepared samples was measured by inductively coupled plasma atomic emission spectrometry (ICP-AES) with an Optima 7000DV Perkin–Elmer instrument.

**Preparation of Cu@C Composites:** In a typical synthesis procedure, D-glucose monohydrate (C<sub>6</sub>H<sub>12</sub>O<sub>6</sub>·H<sub>2</sub>O, 18.9 mmol) was dissolved in distilled water (30 mL) to form a clear solution, and then copper salt {cupric acetate monohydrate [Cu(Ac)<sub>2</sub>·H<sub>2</sub>O], cupric nitrate trihydrate [Cu(NO<sub>3</sub>)<sub>2</sub>·3H<sub>2</sub>O], cupric sulfate pentahydrate [CuSO<sub>4</sub>·5H<sub>2</sub>O], or cupric chloride dihydrate [CuCl<sub>2</sub>·2H<sub>2</sub>O]; 1.89 mmol } was added with stirring to form a light blue solution. The mixture was transferred into a 50 mL Teflon-lined stainless steel autoclave, which was sealed and heated at 180 °C for 0.5–12 h. The solid products were separated by centrifugation, washed with distilled water and absolute ethanol several times, and finally dried at 80 °C for 8 h. Depending on the reaction time, dark red to black solid products could be obtained when Cu(Ac)<sub>2</sub> was used, whereas black solid products were always obtained when other copper salts were used. The as-prepared samples are denoted as CuX-*t*; CuX represents the copper salt used in the synthetic process, and *t* represents the hydrothermal time (h) in the procedure.

**Preparation of CuO@SiO<sub>2</sub> Core–Shell Structure:** Typically, Cu(ac)<sub>2</sub>-12 (0.4 g) was dispersed in a solution composed of ethanol (75 mL), H<sub>2</sub>O (10 mL), NH<sub>3</sub>·H<sub>2</sub>O (25wt.%, 3.8 mL), and *n*-hexadecyltrimethylammonium bromide [C<sub>16</sub>H<sub>33</sub>(CH<sub>3</sub>)<sub>3</sub>NBr, 0.264 g]. The solution was stirred at room temperature for 0.5 h and then dispersed by ultrasound for 0.5 h. TEOS (0.4 mL) was added dropwise to the reaction mixture by using a 1 mL syringe. Then, the mixture was stirred at 500 rpm at room temperature for 8 h. The solid product was separated by centrifugation and washed with distilled water and absolute ethanol three times. The CuO@SiO<sub>2</sub> precursor was dried at 80 °C for 6 h. Finally, the CuO@SiO<sub>2</sub> core–shell structure was obtained after calcination at 600 °C for 6 h.

**Catalytic Activity Test:** The CO + NO reaction was performed with a fixed-bed reactor with a 6 mm diameter glass tube; the catalyst (40–60 mesh; 0.100 g) was set in the reactor by using quartz wool, and gaseous mixtures of 0.8% NO and 0.8% CO diluted with He were blended and fed to the catalyst bed; the NO and CO flow rates were both 23 mL min<sup>-1</sup>. The gas composition was analyzed before and after the reaction by online gas chromatography with a 5A molecular sieves column to separate NO, N<sub>2</sub>, and CO and a Porapak Q column to separate CO<sub>2</sub> and N<sub>2</sub>O. The activity of the CO + NO reaction was evaluated by the following equations:

$$\text{CO conversion \%} = \frac{[\text{CO}]_{\text{in}} - [\text{CO}]_{\text{out}}}{[\text{CO}]_{\text{in}}} \times 100\%$$

$$\text{NO conversion \%} = \frac{[\text{NO}]_{\text{in}} - [\text{NO}]_{\text{out}}}{[\text{NO}]_{\text{in}}} \times 100\%$$

$$\text{N}_2 \text{ yield \%} = 2[\text{N}_2]_{\text{out}}/[\text{NO}]_{\text{in}} \times 100\%$$

$$\text{N}_2\text{O yield \%} = 2[\text{N}_2\text{O}]_{\text{out}}/[\text{NO}]_{\text{in}} \times 100\%$$

[CO]<sub>in</sub> and [NO]<sub>in</sub> are the CO and NO concentrations, respectively, measured before the reaction. [CO]<sub>out</sub>, [NO]<sub>out</sub>, [N<sub>2</sub>]<sub>out</sub>, and [N<sub>2</sub>O]<sub>out</sub> are the CO, NO, N<sub>2</sub>, and N<sub>2</sub>O concentrations, respectively, measured after the reaction.

**Supporting Information** (see footnote on the first page of this article): XRD patterns of samples after TG-DTA measurements; XRD patterns and SEM images of samples prepared with a Cu/glucose molar ratio of 1:5 under different hydrothermal times; SEM images of samples prepared with sucrose and starch; XRD, TG-DTA, copper content, BET surface area, IR and Raman results for different copper sources.

## Acknowledgments

This work was supported by the National Natural Science Foundation of China (NSFC) (20876034), the Program for New Century Excellent Talents in Heilongjiang Provincial University (1155-NCET-014), the Major Foundation of Educational Commission of Heilongjiang Province of China (11531Z11), the Heilongjiang University Natural Science Funds for Distinguished Young Scholars (JCL200802), the Postdoctoral Science-Research Developmental Foundation of Heilongjiang Province of China (LBH-Q12022), the Innovative Research Team in Heilongjiang University (Hdtd2010-10), and the Program for Innovative Research Team in University (IRT-1237).

- a) H. W. Kroto, J. R. Heath, S. C. Brien, R. F. Curl, R. E. Smalley, *Nature* **1985**, *318*, 162–163; b) S. Iijima, *Nature* **1991**, *354*, 56–58.
- a) M. Li, W. Li, S. X. Liu, *Carbohydr. Res.* **2011**, *346*, 999–1004; b) L. H. Ai, J. Jiang, *Mater. Lett.* **2010**, *64*, 1354–1356; c) R. Demir-Cakan, N. Baccile, M. Antonietti, M. M. Titirici, *Chem. Mater.* **2009**, *21*, 484–490; d) X. H. Song, P. Gunawan, R. Jiang, S. S. J. Leong, K. Wang, R. Xu, *J. Hazard. Mater.* **2011**, *194*, 162–168.
- a) Q. Wang, H. Li, L. Q. Chen, X. J. Huang, *Solid State Ionics* **2002**, *152–153*, 43–50; b) Q. Wang, H. Li, L. Q. Chen, X. J. Huang, *Carbon* **2001**, *39*, 2211–2214; c) Y. M. Lu, H. Z. Zhu, W. G. Li, B. Hu, S. H. Yu, *J. Mater. Chem. A* **2013**, *1*, 3783–3788.
- a) H. S. Qian, M. Antonietti, S. H. Yu, *Adv. Funct. Mater.* **2007**, *17*, 637–643; b) A. A. Deshmukh, R. U. Islam, M. J. Witcomb, W. A. L. V. Otterlo, N. J. Coville, *ChemCatChem* **2010**, *2*, 51–54; c) Y. Hu, Y. Liu, H. S. Qian, Z. Q. Li, J. F. Chen, *Langmuir* **2010**, *26*, 18570–18575; d) S. C. Tang, S. Vongehr, Z. Zheng, H. J. Liu, X. K. Meng, *J. Phys. Chem. C* **2010**, *114*, 18338–18346; e) R. Z. Yang, H. Li, X. P. Qiu, L. Q. Chen, *Chem. Eur. J.* **2006**, *12*, 4083–4090; f) L. R. Kong, X. F. Lu, X. J. Bian, W. J. Zhang, C. Wang, *Langmuir* **2010**, *26*, 5985–5990; g) M. B. Zheng, J. M. Cao, X. Chang, J. Wang, J. S. Liu, X. J. Ma, *Mater. Lett.* **2006**, *60*, 2991–2993; h) X. M. Sun, Y. D. Li, *Angew. Chem.* **2004**, *116*, 3915; *Angew. Chem. Int. Ed.* **2004**, *43*, 3827–3831; i) X. L. Li, T. J. Lou, X. M. Sun, Y. D. Li, *Inorg. Chem.* **2004**, *43*, 5442–5449.
- a) W. M. Qiao, Y. Song, S. Y. Lim, S. H. Hong, S. H. Yoon, *Carbon* **2006**, *44*, 158–193; b) Y. S. Hu, R. Demir-Cakan, M. M. Titirici, J. O. Muller, R. Schlogl, M. Antonietti, J. Maier, *Angew. Chem.* **2008**, *120*, 1669; *Angew. Chem. Int. Ed.* **2008**, *47*, 1645–1649; c) C. D. Liang, Z. J. Li, S. Dai, *Angew. Chem.* **2008**, *120*, 3754; *Angew. Chem. Int. Ed.* **2008**, *47*, 3696–3717.
- a) B. Hu, K. Wang, L. H. Wu, S. H. Yu, M. Antonietti, M. M. Titirici, *Adv. Mater.* **2010**, *22*, 813–828; b) B. Hu, S. H. Yu, K. Wang, L. Liu, X. W. Xu, *Dalton Trans.* **2008**, *40*, 5414–5423.
- a) M. M. Titirici, A. Thomas, S. H. Yu, J. O. Muller, M. Antonietti, *Chem. Mater.* **2007**, *19*, 4205–4212; b) X. M. Sun, Y. D. Li, *Angew. Chem.* **2004**, *116*, 607; *Angew. Chem. Int. Ed.* **2004**, *43*, 597–601; c) Y. Z. Mi, W. B. Hu, Y. M. Dan, Y. L. Liu, *Mater. Lett.* **2008**, *62*, 1194–1196; d) M. Sevilla, A. B. Fuertes, *Chem. Eur. J.* **2009**, *15*, 4195–4203.

- [8] C. Yao, Y. Shin, L. Q. Wang, C. F. Windisch, W. D. Samuels, B. W. Arey, C. M. Wang, W. M. Risen, G. J. Exarhos, *J. Phys. Chem. C* **2007**, *111*, 15141–15145.
- [9] Y. Shin, L. Q. Wang, I. T. Bae, B. W. Arey, G. J. Exarhos, *J. Phys. Chem. C* **2008**, *112*, 14236–14240.
- [10] a) M. T. Zheng, Y. L. Liu, Y. Xiao, Y. Zhu, Q. Guan, D. S. Yuan, J. X. Zhang, *J. Phys. Chem. C* **2009**, *113*, 8455–8459; b) M. Sevilla, A. B. Fuertes, *Carbon* **2009**, *47*, 2281–2289.
- [11] a) M. M. Titirici, M. Antonietti, A. Thomas, *Chem. Mater.* **2006**, *18*, 3808–3812; b) Z. M. Li, X. Y. Lai, H. Wang, D. Mao, C. J. Xing, D. Wang, *J. Phys. Chem. C* **2009**, *113*, 2792–2797; c) Y. F. Zhu, E. Kockrick, T. Ikoma, N. Hanagata, S. Kaskel, *Chem. Mater.* **2009**, *21*, 2547–2553; d) Y. F. Zhu, T. Ikoma, N. Hanagata, S. Kaskel, *Small* **2010**, *6*, 471–478.
- [12] M. M. Titirici, A. Thomas, M. Antonietti, *New J. Chem.* **2007**, *31*, 787–789.
- [13] a) Z. F. Wang, P. F. Xiao, N. Y. He, *Carbon* **2006**, *44*, 3277–3284; b) G. X. Zhu, X. W. Wei, S. Jiang, *J. Mater. Chem.* **2007**, *17*, 2301–2306; c) W. H. Xu, S. H. Yu, *Small* **2009**, *5*, 460–465; d) S. R. Guo, J. Y. Gong, P. Jiang, M. Wu, Y. Lu, S. H. Yu, *Adv. Funct. Mater.* **2008**, *18*, 872–879; e) S. I. Gai, P. P. Yang, C. X. Li, W. X. Wang, Y. L. Dai, N. Niu, J. Lin, *Adv. Funct. Mater.* **2010**, *20*, 1166–1172; f) S. Ikeda, Y. Ikoma, H. Kobayashi, T. Harada, T. Torimoto, B. Ohtanic, M. Matsumura, *Chem. Commun.* **2007**, *36*, 3753–3755; g) S. C. Tang, V. Sascha, X. K. Meng, *J. Phys. Chem. C* **2010**, *114*, 977–983; h) P. Makowski, R. Demir-Cakan, M. Antonietti, F. Goettmann, M. M. Titirici, *Chem. Commun.* **2008**, *8*, 999–1001.
- [14] a) G. B. Yu, B. Sun, Y. Pei, S. H. Xie, S. R. Yan, M. H. Qiao, K. N. Fan, X. X. Zhang, B. N. Zong, *J. Am. Chem. Soc.* **2010**, *132*, 935–937; b) R. D. Cakan, M. M. Titirici, M. Antonietti, G. L. Cui, J. Maier, Y. S. Hu, *Chem. Commun.* **2008**, 3759–3761; c) X. J. Cui, M. Antonietti, S. H. Yu, *Small* **2006**, *2*, 756–759.
- [15] B. M. Nagaraja, A. H. Padmasri, B. D. Raju, K. S. R. Rao, *J. Mol. Catal. A* **2007**, *265*, 90–97.
- [16] a) J. Y. Gong, S. H. Yu, H. S. Qian, L. B. Luo, T. W. Li, *J. Phys. Chem. C* **2007**, *111*, 2490–2496; b) W. H. Xu, Y. X. Zhang, Z. Guo, X. Chen, J. H. Liu, X. J. Huang, S. H. Yu, *Small* **2012**, *8*, 53–58; c) H. Y. Zhao, Y. F. Wang, J. H. Zeng, *Cryst. Growth Des.* **2008**, *8*, 3731–3734; d) Q. W. Zhu, Y. H. Zhang, J. J. Wang, F. S. Zhou, P. K. Chu, *J. Mater. Sci. Technol.* **2011**, *27*, 289–295; e) X. X. Zhang, J. M. Song, J. Jiao, X. F. Mei, *Solid State Sci.* **2010**, *12*, 1215–1219.
- [17] Y. F. Wang, A. V. Biradar, G. Wang, K. K. Sharma, C. T. Duncan, S. Rangan, T. Asefa, *Chem. Eur. J.* **2010**, *16*, 10735–10743.
- [18] Z. C. Orel, A. Anzlovar, G. Drazic, M. Zigon, *Cryst. Growth Des.* **2007**, *7*, 453–458.
- [19] M. T. Zheng, Y. L. Liu, K. M. Jiang, Y. Xiao, D. S. Yuan, *Carbon* **2010**, *48*, 1224–1233.
- [20] a) M. Zahmakiran, S. Ozkar, *Mater. Lett.* **2009**, *63*, 1033–1036; b) J. Li, Y. Shi, Q. Cai, Q. Y. Sun, H. D. Li, X. H. Chen, X. P. Wang, Y. J. Yan, E. G. Vrieling, *Cryst. Growth Des.* **2008**, *8*, 2652–2659.
- [21] C. Sheng, *Fuel* **2007**, *86*, 2316–2324.
- [22] K. S. W. Sing, D. H. Everett, R. A. W. Haul, L. Moscou, R. A. Pierotti, J. Rouquerol, T. Siemieniowska, *Pure Appl. Chem.* **1985**, *57*, 603–619.

Received: May 14, 2013  
Published Online: July 30, 2013